Journal of Materials Chemistry A

ROYAL SOCIETY OF CHEMISTRY

PAPER

View Article Online
View Journal

Cite this: DOI: 10.1039/d5ta08061d

Electrochemical lithiation of the layered superionic conductors $AgCrSe_2$ and $CuCrSe_2$

Seongbak Moon,[a] Md Towhidur Rahman,[c] Noah P. Holzapfel,[a] Alexandra Zevalkink[b] and Veronica Augustyn *[a]

The layered transition metal chalcogenides $MCrX_2$ (M = Ag, Cu; X = S, Se, Te) are of interest for energy storage because chemically Li-substituted analogs were reported as superionic Li^+ conductors. The coexistence of fast ion transport and reducible transition metal and chalcogen elements suggests that this family may offer multifunctional capability for electrochemical storage. Here, we investigate the electrochemical reduction of $AgCrSe_2$ and $CuCrSe_2$ in non-aqueous Li- and Na-ion electrolytes using electrochemical measurements coupled with *ex situ* characterization (scanning electron microscopy, energy-dispersive X-ray spectroscopy, X-ray diffraction, and X-ray photoelectron spectroscopy). Both compounds delivered high initial specific capacities (~560 mAh g^{-1}), corresponding to 6.6 and 5.7 Li^+/e^- per formula unit for $AgCrSe_2$ and $CuCrSe_2$, respectively. We attribute this difference to distinct reduction pathways: (1) Li^+ intercalation to form $LiCrSe_2$ and extruded Ag or Cu, (2) conversion of $LiCrSe_2$ to Li_2Se, and (3) formation of an Ag–Li alloy at the lowest potential, operative only in $AgCrSe_2$. Consistent with this proposed mechanism, step 3 was absent during reduction of $AgCrSe_2$ in a Na-ion electrolyte since Ag does not alloy with Na. These results demonstrate the complex reduction chemistry of $MCrX_2$ in the presence of alkali ions, providing insights into the use of $MCrX_2$ materials as alkali ion superionic conductors or high capacity electrodes for lithium or sodium-ion type batteries.

Received 1st October 2025
Accepted 13th December 2025

DOI: 10.1039/d5ta08061d

rsc.li/materials-a

1. Introduction

The ever-increasing demand for high energy density lithium-ion rechargeable batteries motivates the search for new types of high capacity electrode materials. On the anode side, this includes metallic anodes such as lithium metal, alloying-type anodes such as silicon, and a broad range of compounds including those based on transition metal chalcogenides that undergo conversion-type reaction mechanisms.[1–3] Conversion-type electrodes achieve higher specific capacities than insertion-type electrodes because they can undergo a greater degree of charge transfer involving large microstructural transformations. Transition metal chalcogenides are one class of conversion-type electrodes, which upon lithiation, undergo multi-step reactions involving Li^+ intercalation followed by conversion to metal nanoparticles and Li_2X (X = S, Se, Te).[4–7] While such reactions lead to high capacities they are often accompanied by poor electronic conductivity,[8–10] significant volume changes,[11–13] and dissolution[14,15] of reaction intermediates. Nevertheless, their redox-active metal centers and tunable interlayer spacing render the materials as valuable model systems for understanding conversion mechanisms. Insights from transition metal chalcogenides provide a useful comparative framework for evaluating less-explored layered materials like $MCrX_2$ (M = Ag, Cu; X = S, Se, Te). With M in the structure, we can anticipate additional reduction mechanisms possible through extrusion, as reported for Fe-doped CeO_2.[16]

High ionic conductivity is an important characteristic for solid-state electrolytes and mixed ionic-electronic electrode materials for battery applications. $MCrX_2$ (M = transition metal and X = chalcogenide) is a class of layered materials that exhibit superionic conductivity of the M cation upon an order–disorder transition at elevated temperatures. This dynamic disorder in the cation sublattice not only enables fast ion transport but also suppresses lattice thermal conductivity, making these materials attractive for both solid-state electrolyte and thermoelectric applications.[17–19] In addition to intrinsic M^+ conductivity, the partial substitution of M^+ with Li^+ was reported in $AgCrS_2$.[20] The proposed lithiated $Li_{0.31}Ag_{0.69}CrS_2$ had an ionic conductivity of 19.6 mS cm^{-1} at 298 K, greater than that of standard liquid lithium-ion battery electrolytes (~10 mS cm^{-1}). This result suggested the tantalizing possibility of Li^+ solid state superionic conductors formed simply through partial ion exchange of Ag^+ with Li^+, although the method employed a strong chemical reducing agent, *tert*-butyllithium. This finding raised the question of the exact mechanism of Li^+ substitution into $AgCrS_2$

[a]*Department of Materials Science and Engineering, North Carolina State University, Raleigh, NC 27695, USA. E-mail: vaugust@ncsu.edu*

[b]*Department of Chemical Engineering and Materials Science, Michigan State University, East Lansing, MI 48824, USA*

[c]*Department of Mechanical Engineering, Michigan State University, East Lansing, MI 48824, USA*

in reducing conditions. While the electrochemical behavior of conventional transition metal chalcogenides has been broadly characterized, prior studies on $MCrX_2$ materials have mainly centered on their cation superionic conductivity rather than their reduction chemistry. In this context, examining the electrochemical reduction of $AgCrSe_2$ and $CuCrSe_2$ provides information that can be considered alongside what is known for other layered chalcogenide systems. To the best of our knowledge, there is no prior work on the chemical or electrochemical reduction mechanism of $AgCrSe_2$ and related materials. Therefore, we decided to investigate the electrochemical behavior of this class of materials to determine whether Li^+/Ag^+ substitution is possible, as well as whether this class of materials exhibits promising electrochemical properties for non-aqueous rechargeable batteries.

In this work, we performed electrochemical reduction of $AgCrSe_2$ and $CuCrSe_2$ in non-aqueous lithium and sodium-ion electrolytes. We analyzed the electrochemical behavior together with a suite of *ex situ* characterization techniques, including scanning electron microscopy (SEM), energy-dispersive X-ray spectroscopy (EDS), X-ray diffraction (XRD), and X-ray photoelectron spectroscopy (XPS). $AgCrSe_2$ had a maximum capacity of 560 mAh g^{-1} corresponding to the storage of 6.6 electrons and Li^+ per $AgCrSe_2$. We identified three sequential lithium-ion coupled electron transfer reduction mechanisms in $AgCrSe_2$: (1) Li intercalation to form $LiCrSe_2$ and with the exsolution of Ag^0,nd (2) a conversion reaction to form Li_2Se, and (3) an Ag–Li alloying reaction. For $CuCrSe_2$ in Li^+ and $AgCrSe_2$ in a Na^+ electrolyte, reaction (3) was absent due to the lack of possible Cu–Li and Ag–Na alloying. We found only limited Li^+ substitution into $AgCrSe_2$, and it was concomitant with the formation of Ag^0 at the surface.

2. Experimental methods

2.1. Chemicals

All chemicals were used as received. Silver (Ag; shot, 99.99%), chromium (Cr; chips, 99.995%), *n*-methyl-2-pyrrolidone (NMP; anhydrous), lithium perchlorate ($LiClO_4$; anhydrous, battery grade), propylene carbonate (PC; anhydrous), and 1.0 M lithium hexafluorophosphate in ethylene carbonate/dimethyl carbonate [$LiPF_6$ in EC/DMC, 50/50 (v/v)] were purchased from Millipore-Sigma. Copper (Cu; powder, 99.9%), selenium (Se; shot, 99.999%), and acetylene black (100% compressed) were purchased from Fisher Scientific. Polyvinylidene fluoride (PVDF; Kynar HSV 900) was obtained from Arkema Inc. Cu foil (9 μm thick) was purchased from MTI Corp.

2.2. Material synthesis

Polycrystalline $AgCrSe_2$ and $CuCrSe_2$ were synthesized by solid state reaction. The corresponding stoichiometric amounts of Ag (shot, Sigma-Aldrich, 99.99% purity), Cr (chips, Sigma-Aldrich, 99.995% purity), and Se (shot, Alfa-Aesar, 99.999% purity) were weighed in an argon-filled glovebox. For $AgCrSe_2$, the weighted elements were sealed in a quartz ampoule under static vacuum, heated up to 1173 K at 1 K per minute rate for 24 hours, followed by slow cooling in 12 hours, and finally hand-ground by mortar and pestle into fine powder inside the glovebox. Phase purity of the obtained powder was confirmed with XRD. The synthesis of $CuCrSe_2$ involved an initial ball-milling step, which is reported to help avoid formation of $CuCr_2Se_4$ as a secondary phase. The elemental precursors were sealed in stainless steel SPEX vials inside of an argon-filled glovebox. 10 g of powder were then ball milled with three 7/16″-stainless steel ball bearings for 3 hours using a ball mill (SPEX SamplePrep 8000D). After milling, approximately 93% of the initial load was recovered. The powder was vacuum sealed in a quartz ampoule, heated to 973 K, held for 4 hours and air quenched. Lastly, the sample was ground by mortar and pestle and sintered in a spark plasma sintering press at 873 K for 20 minutes to obtain a phase-pure consolidated sample, which was later crushed into fine powder for electrode preparation. $AgCrSe_2$ and $CuCrSe_2$ are moderately air sensitive and show oxidation after several hours to days of exposure. To minimize exposure, the samples were synthesized in an inert atmosphere and stored in an argon-filled glovebox.

2.3. Electrode preparation

$AgCrSe_2$ and $CuCrSe_2$ powders were mixed with acetylene black and PVDF in a weight ratio of 8 : 1 : 1 in NMP solvent. Electrodes were prepared by drop-casting the slurry onto a 1.13 cm^2 area of Cu foil for an active material mass loading of ~1.6 mg cm^{-2} for electrochemical characterization and ~5.7 mg cm^{-2} for *ex situ* and *operando* electrochemical XRD characterization. All slurry mixing and drop-casting steps were carried out outside the glovebox. The electrodes were dried at 60 °C for 12 h in air followed by 120 °C for 12 h under vacuum prior to transfer into an argon-filled glovebox (MBraun Labstar Pro) for coin cell assembly.

2.4. Electrochemical characterization

Coin cells (CR2032, MTI Corp.) were fabricated inside an argon-filled glovebox (MBraun Labstar Pro) with Ar and H_2O levels < 1 ppm. The cathode consisted of the $AgCrSe_2$ or $CuCrSe_2$ porous composite electrode, while a metallic Li chip was used as the anode. The electrolyte was 1.0 M $LiPF_6$ in EC/DMC (50 : 50, v/v) or 1.0 M $LiClO_4$ in PC. For the Na system, Na metal was used as the anode with 1.0 M $NaClO_4$ in PC. A glass microfiber filter (GF/F, Whatman) was used as the separator. The coin cells were crimped with a pressure of 0.8 torr using a digital pressure controlled electric crimper (MSK-160E, MTI Corp.). Electrochemical characterization methods, including galvanostatic cycling with potential limitation (GCPL), galvanostatic intermittent titration technique (GITT), and electrochemical impedance spectroscopy (EIS), were conducted using a potentiostat (BioLogic VMP3). GCPL was performed with a constant applied current of 10 mA g^{-1} to different lower cut-off potentials: 2.1, 1.5, 0.8, and 0.1.

2.5. Physical characterization

Standard powder and *ex situ* powder XRD were performed using a Rigaku SmartLab X-ray diffractometer in Bragg–Brentano

geometry with Cu Kα radiation (λ = 1.5406 Å). Samples for *ex situ* XRD were prepared in an argon-filled glovebox in a coin cell (MTI Corporation) with 8 μm Kapton film window (Spex CertiPrep). Scanning electron microscopy (SEM) measurements were performed on a Hitachi SU8700 field-emission scanning electron microscope equipped with Oxford energy dispersive X-ray spectrometer (EDS) detector. *Ex situ* samples were prepared in an argon-filled glovebox in a plastic sample holder sealed with Parafilm. During loading, samples were exposed to the ambient for approximately 2 minutes. SEM images and EDS mapping data were collected at 5 keV and 20 keV, respectively. X-ray photoelectron spectroscopy (XPS) measurements were conducted on a SPECS PHOIBOS 150. Pristine and *ex situ* electrodes on Cu foil were attached to the stainless steel sample holder in an argon-filled glovebox using carbon tape. During loading, samples were exposed to the ambient for approximately 1 minute.

2.6. *Operando* electrochemical X-ray diffraction (EC-XRD)

Operando EC-XRD of $AgCrSe_2$ was collected on a PANalytical X'Pert powder diffractometer (45 kV, 40 mA, sealed Cu tube, $K\alpha_1$ λ = 1.5406 Å, $K\alpha_2$ λ = 1.5444 Å) with a coin cell stage and X'Celerator position-sensitive detector in Bragg–Brentano geometry. Li-metal half-cells (CR2032) consisted of an anode casing, spring, two spacers, 8 mm Li disk, and glass fiber separator with 120 μL of 1 M $LiClO_4$ in PC. Composite slurry electrodes (3.8 mg cm^{-2}) were coated onto stainless steel mesh, dried at 120 °C under vacuum, and punched into 19 mm disks. The cathode casing had a 7 mm hole covered with 8 μm Kapton film. PXRD patterns were collected from 20°–43° 2θ (0.033° step, 7 min scan). Cells were discharged at 30 mA g^{-1} for one cycle.

3. Discussion

We characterized the crystal structure and microstructure of the synthesized (Ag,Cu)$CrSe_2$ with XRD and SEM, respectively. Rietveld refinement of the structural models based on the XRD data (Fig. 1a and b) confirmed that both $AgCrSe_2$ and $CuCrSe_2$ crystallize in a rhombohedral structure (space group *R*3*m*) without detectable secondary phases or impurities. The refined lattice parameters were a = 3.6760(1) Å and c = 19.3854(2) Å for $CuCrSe_2$, and a = 3.6803(1) Å and c = 21.2170(7) Å for $AgCrSe_2$. The larger c-axis of $AgCrSe_2$ reflects the larger ionic radius of Ag^+ compared to Cu^+, leading to an expanded interlayer spacing. The low R_{wp} values (1.54% for $CuCrSe_2$ and 1.90% for $AgCrSe_2$) indicate excellent agreement between the observed and calculated patterns. Both structures exhibited high crystallinity, as indicated by the sharp diffraction peaks and low background noise. These results confirm the successful synthesis of the

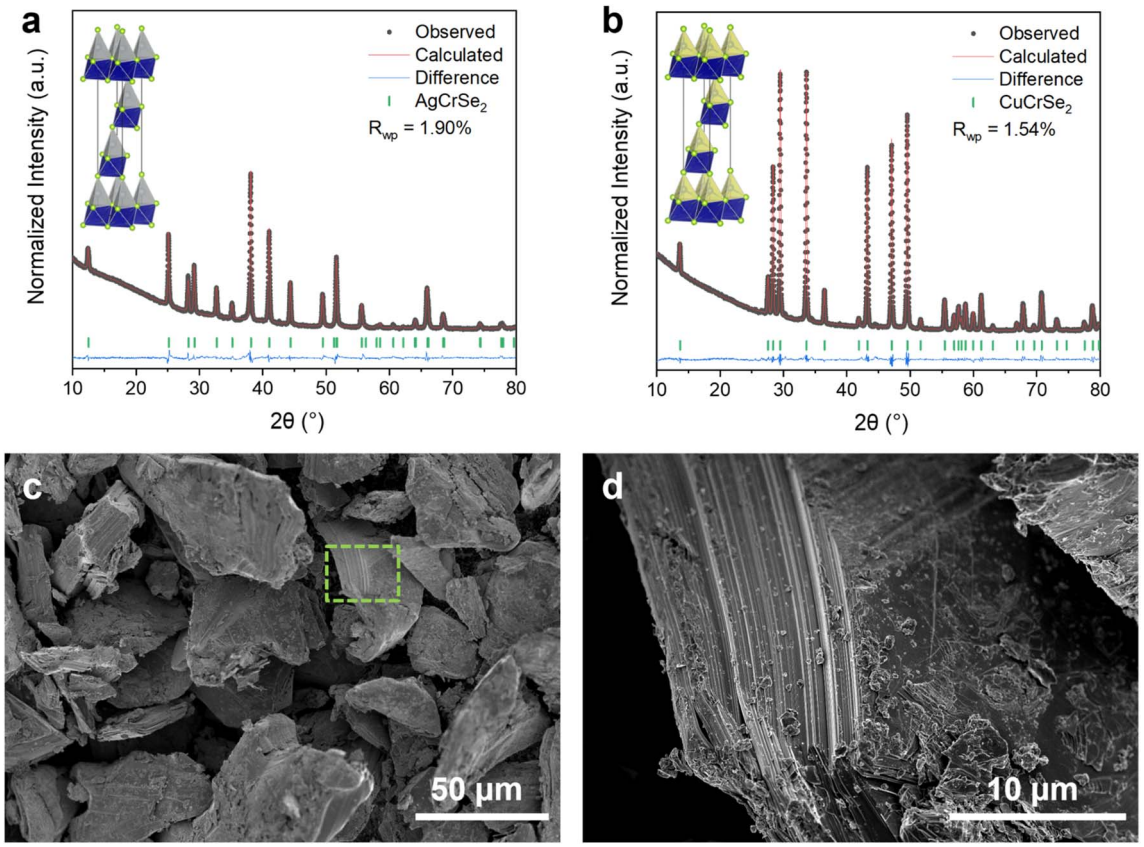

Fig. 1 Rietveld refinement of the structural models based on the XRD data collected for (a) $AgCrSe_2$ and (b) $CuCrSe_2$, confirming phase-pure rhombohedral *R*3*m* structure with high crystallinity; insets show the corresponding refined crystal structures. (c) SEM image of $AgCrSe_2$ particles, revealing non-uniform tens-μm morphology. (d) Magnified view of the region marked in (c), highlighting layered striated features consistent with the crystalline framework.

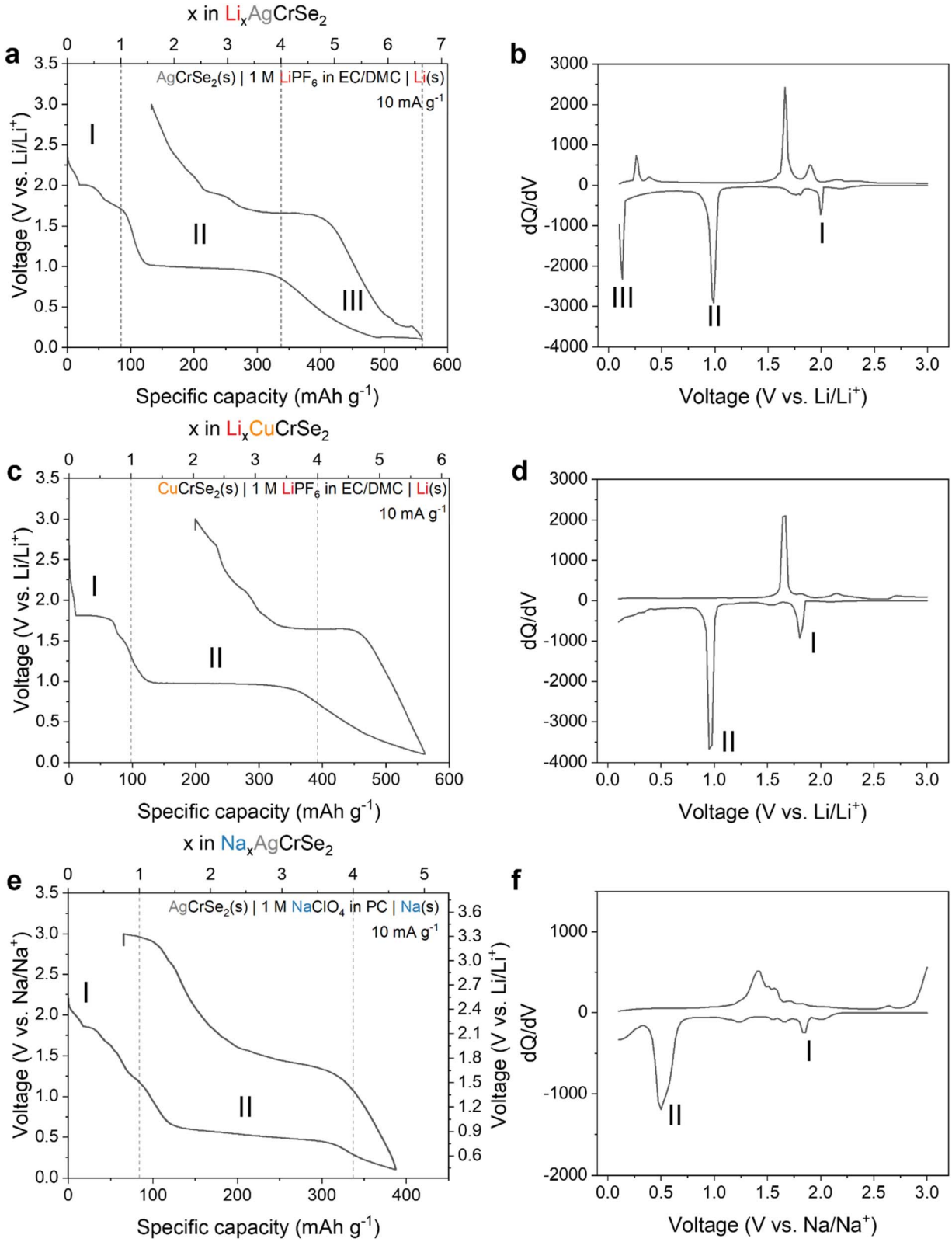

Fig. 2 Galvanostatic profiles at 10 mA g^{-1} and corresponding differential capacity plots. (a and b) Lithiation of $AgCrSe_2$ shows three reduction regions (~2.0, 1.0, 0.13 V) that suggest stepwise processes. (c and d) Lithiation of $CuCrSe_2$ displays two main regions, lacking the low-voltage feature seen in $AgCrSe_2$. (e and f) Sodiation of $AgCrSe_2$ shows two plateaus (~2.15, 1.0 V), consistent with the absence of a low-voltage alloying step.

phase-pure layered chalcogenides, suitable for further studies on their electrochemical or transport properties.[21] The morphology of the synthesized $AgCrSe_2$ consists of non uniform particles with sizes on the order of tens of micrometers (Fig. 1c). A zoomed-in view of the side of a particle reveals the layered crystalline structure as indicated by the uniform striation features along the block facet (Fig. 1d).

3.1. Mechanism of electrochemical reduction

Next we considered the electrochemical behavior of the layered (Ag,Cu)$CrSe_2$ in Li-ion and Na-ion non-aqueous electrolytes, respectively, for which there are no prior reports. These studies allowed us to determine the electrochemical behavior as a function of the transition metal (Ag^+ *vs.* Cu^+) and charge-compensating cation in the electrolyte (Li^+ *vs.* Na^+). The first galvanostatic discharge and charge cycles under the various conditions tested are shown in Fig. 2. First we consider the reduction of $AgCrSe_2$ to 0.1 V in a Li^+-containing electrolyte, which is associated with a specific capacity of 560 mAh g^{-1}. Assuming that the electrochemical reduction is accompanied by a Li^+ cation (Li^+-coupled electron transfer), this corresponds to the transfer of 6.6 Li^+, e^- per $AgCrSe_2$. Upon oxidation, the capacity is 427 mAh g^{-1} (5.1 Li^+, e^- per $AgCrSe_2$), indicating that ~76% of the charge is reversible. Based on the number of plateau regions in the discharge profile and corresponding number of peaks in the differential capacity (dQ/dV) plot, we propose a three-step mechanism (regions I–III, labeled in Fig. 2a) for the electrochemical reduction of $AgCrSe_2$ in a non-aqueous Li^+ electrolyte.

Region I is associated with a one electron reduction process consisting of multiple shoulder plateaus around 2.0 V, which may include Ag^+ extrusion and Li^+ insertion processes that cannot be clearly separated in the voltage profile. Region II is associated with a reduction step requiring the transfer of three electrons and a flat voltage profile near 1.0 V, while region III is associated with the remaining 2.6 electrons and a sloping voltage profile followed by a third plateau above 0.1 V. The three distinct reduction steps can also be identified from the differential capacity (dQ/dV) plot (Fig. 2b), corresponding to three distinct reduction peaks at 2.0 V, 1.0 V, and 0.13 V. To help us develop a mechanism for the electrochemical reduction of $AgCrSe_2$ with Li^+, we evaluated the reversibility of the electrochemical reactions by using galvanostatic cycling with decreasing cathodic potential cutoffs (Fig. S1, and Table 1). We quantified the reversibility in terms of the degree of electron transfer (coulombic efficiency) and voltage (voltage hysteresis) during reduction and oxidation. Between 3.0 and 2.1 V (region I), $AgCrSe_2$ shows reversible electrochemical behavior as characterized by high average coulombic efficiency (99.8%) and negligible voltage hysteresis. Expanding the range to 3.0–1.5 V completes the voltage plateau at 2.0 V (region I), but leads to lower coulombic efficiency (98.3%) and a greater voltage hysteresis of ~0.2 V. Lowering the potential further to 0.8 V leads to the appearance of the voltage plateau at 1.0 V (region II), with a coulombic efficiency of 89.1% and a voltage hysteresis of 0.7 V. Finally, further decreasing it to 0.1 V (region III) leads to the appearance of a sloping region from 1.0 to 0.13 V, followed by an additional plateau at 0.13 V, with a coulombic efficiency of 96.6% and a voltage hysteresis of approximately 0.2 V. Based on these features, we propose that the electrochemical reduction of $AgCrSe_2$ in a Li^+-containing non-aqueous electrolyte proceeds as follows:

$$AgCrSe_2 + Li^+ + e^- \rightarrow Ag + LiCrSe_2 \quad (1)$$

$$LiCrSe_2 + 3Li^+ + 3e^- \rightarrow Cr + 2Li_2Se \quad (2)$$

$$Ag + 2.6Li^+ + 2.6e^- \rightarrow Li_{2.6}Ag \quad (3)$$

Evidence supporting this proposed mechanism is presented in the following sections. The Li–Ag alloying reaction occurs at approximately 0.28 V.[22]

To help evaluate the proposed mechanism for $AgCrSe_2$ lithiation, we performed electrochemical reduction of $CuCrSe_2$ in a non-aqueous Li^+ electrolyte (Fig. 2c). The first cycle reduction capacity was 562 mAh g^{-1}, which corresponds to approximately 5.7 e^-, Li^+ per $CuCrSe_2$, which is almost 1 electron less than the capacity obtained for the Ag-analog. We hypothesized that, since Step I involves replacing the monovalent metal ions (Ag^+ and Cu^+) with Li^+, there would be no change in the degree of lithiation per formula unit. This holds even though the first voltage plateau for $CuCrSe_2$ appears at 1.8 V, approximately 0.2 V lower than that for $AgCrSe_2$. This is in line with the lower standard reduction potential of Cu^+ *vs.* Ag^+.[23] The plateau at 1.0 V is the same as in $AgCrSe_2$. Since it likely corresponds to the conversion of $LiCrSe_2$ to Li_2Se and Cr (step II), these reactions are the same in $CuCrSe_2$ and $AgCrSe_2$, and so the voltage plateau is unchanged. Reduction of $AgCrSe_2$ to 0.13 V, just before the third plateau, delivers 484 mAh g^{-1} (5.7 Li^+ per $AgCrSe_2$), compared to 562 mAh g^{-1} (5.7 Li^+ per $CuCrSe_2$). This indicates that the same amount of Li^+ per (Ag or Cu)$CrSe_2$ participates in the reaction before the assumed Li–Ag alloying. This reinforces our assumption that step III includes the Li–Ag alloying reaction. Finally, the smaller discharge capacity and absence of the third reaction plateau in $CuCrSe_2$ may be attributed to the fact that Cu does not alloy with Li, unlike Ag. This is clearly shown in Fig. 2d by the absence of the third reduction peak.

Next we investigated the role of the charge compensating cation in the electrolyte by performing electrochemical characterization in a non-aqueous Na^+-containing electrolyte. Reduction of $AgCrSe_2$ under these conditions (Fig. 2e) shows two primary voltage plateaus, at 2.15 and 1.0 V *vs.* Na/Na^+ (1.85

Table 1 Electrochemical summary of $AgCrSe_2$ across different voltage ranges: curve shape, voltage hysteresis, and coulombic efficiency

Voltage range (V)	Curve shape	Voltage hysteresis (V)	Coulombic efficiency (%)
3.0–2.1	Sloping	Negligible	99.8
3.0–1.5	Plateau	0.2	98.3
3.0–0.8	Plateau	0.7	89.1
3.0–0.1	Plateau	0.2	96.6

and 0.7 V *vs.* Li/Li^+). The loss of the third and lowest potential plateau is attributed to the inability of Na to alloy with Ag.[24] The second voltage plateau, starting near 1.0 V, is likely related to the following conversion reaction:

$$NaCrSe_2 + 3Na^+ + 3e^- \rightarrow 2Na_2Se + Cr \quad (4)$$

3.2. Morphological and compositional changes during lithiation

Our proposed mechanism, involving metal exsolution, conversion, and alloying, should lead to significant changes in the microstructure, crystal structure, and surface composition of the electrodes. To that end, we performed *ex situ* SEM, EDS, XRD, and XPS characterization of $AgCrSe_2$ at different states of charge. Porous $AgCrSe_2$ electrodes were discharged at 10 mA g^{-1} to 2.1 V, 1.5 V, 0.8 V, and 0.1 V, followed by chronoamperometry at each potential for 12 hours to ensure completion of the electrochemical reaction. The *ex situ* SEM images in Fig. 3 demonstrate the expected morphological changes during lithiation. Pristine $AgCrSe_2$ has a layered microstructure. By 2.1 V, small particles appeared on the surface of the material while at 1.5 V, the surface became extensively covered by these particles that grew and accumulated, indicating progressive surface reconstruction during lithiation. Further reduction to 0.8 V led to growth of the overlayer, creating a rugged surface, and by 0.1 V, these valleys and lower surfaces were filled, resulting in a flatter appearance. These microstructural changes indicate a progressive transformation of the electrode material, with surface particle formation and growth likely driven by Ag

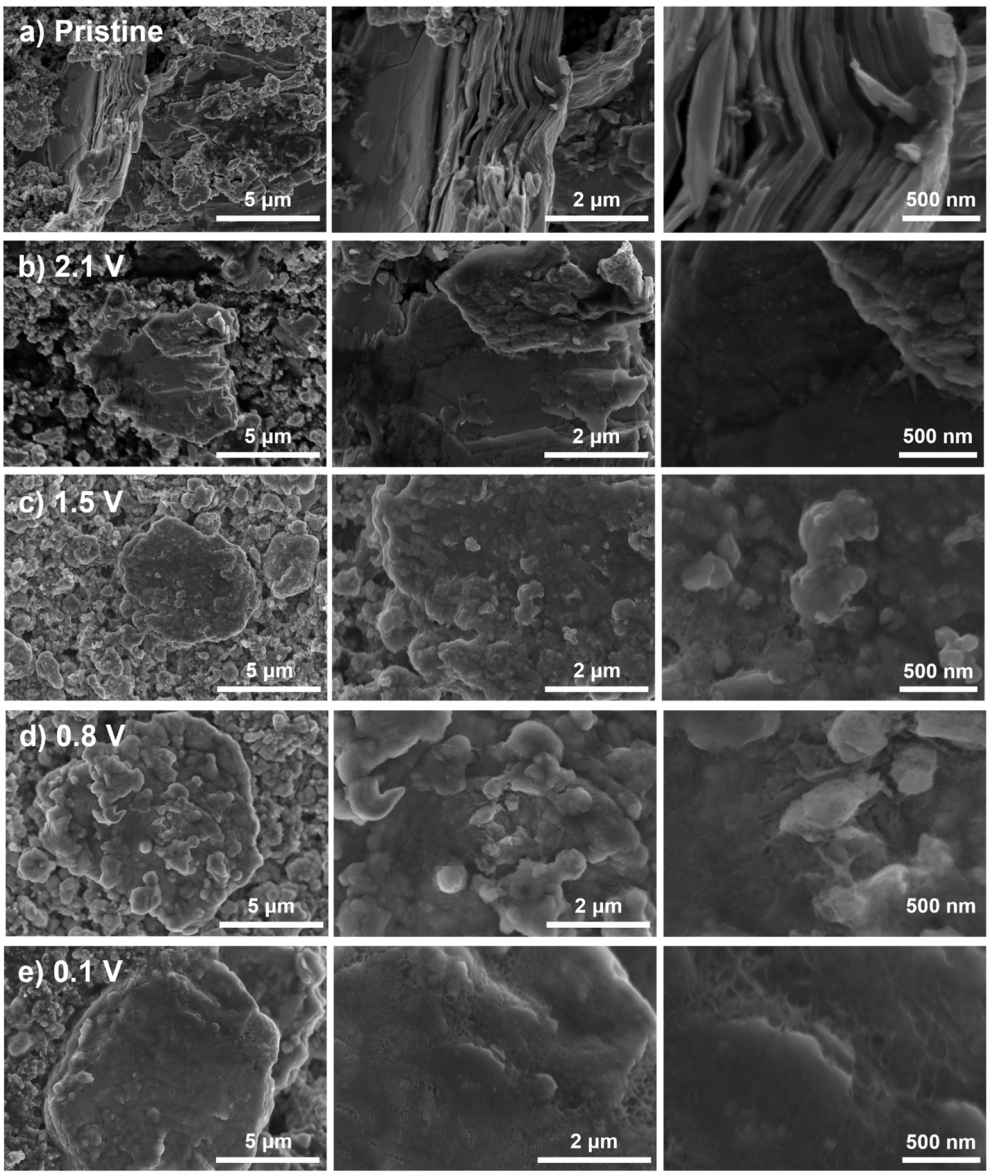

Fig. 3 *Ex situ* SEM images of $AgCrSe_2$ electrodes during electrochemical reduction in a non-aqueous Li^+ electrolyte to different lower cutoff voltages: (a) pristine, (b) 2.1 V, (c) 1.5 V, (d) 0.8 V, and (e) 0.1 V, showing progressive surface reconstruction with the emergence and growth of Ag nanoparticles consistent with the proposed extrusion–conversion–alloying mechanism.

extrusion and Li^+ insertion. The associated microstructural evolution, including phase transitions and possible rearrangement of the $AgCrSe_2$ framework, remains to be clarified, particularly whether Ag de-insertion and Li^+ insertion occur simultaneously or in distinct steps.

We performed *ex situ* energy dispersive X-ray spectroscopy (EDS) to analyze the distribution of Ag, Cr, and Se. All three elements were evenly distributed throughout the material in pristine $AgCrSe_2$ (Fig. S2). Upon discharge to 2.1 V, we found regions with high Ag intensity and the absence of Cr and Se. At 1.5 V, these intensity differences became more pronounced, indicating further changes in elemental distribution. At 0.8 V and 0.1 V, scattered Ag intensity spots were observed, with lower Cr and Se intensities at those spots. The redistribution of Ag further indicates an exsolution process occurring in $AgCrSe_2$. This could proceed *via* a nucleation and growth mechanism, whereby Ag clusters form and coalesce into distinct, localized spots, separating from the lattice (Fig. S2d and e). In contrast, Cr does not form a distinct phase, which may explain why it is not observed in EDS. This is possibly due to the limited diffusion of Cr atoms, residual Cr–Se interactions, or amorphous phase formation.

Fig. S2 and Table S1 show the EDS oxygen mapping results of the *ex situ* samples at each cutoff voltage after approximately two minutes of air exposure. The signal intensity increases with deeper lithiation, likely due to the higher reactivity of more reduced samples under ambient conditions. This trend is quantitatively confirmed by the atomic percentage data, which show an increase in the oxygen to carbon ratio (O : C) from 0.03 in the pristine sample to 0.29 in the 0.1 V sample.

3.3. Structural evolution during lithiation

We performed *ex situ* X-ray diffraction (XRD) of the $AgCrSe_2$ porous electrode at various cutoff voltages using an airtight cell with a Kapton window to prevent air exposure, since the reduced electrode is air sensitive (Fig. 4). The XRD pattern of pristine $AgCrSe_2$ powder matched well with the previously reported pattern.[25,26] In the porous electrode on a Cu foil substrate, Cu peaks dominated but the $AgCrSe_2$ peaks remained visible. At 2.1 V, new peaks corresponding to $LiCrSe_2$ appeared around 32° and 40° 2θ. The *ex situ* sample, marked as 2.1 V was discharged to 2.1 V and subsequently held at 2.1 V by chronoamperometry for about 4 hours. Based on the specific capacity, this corresponds to $Li_{0.21}AgCrSe_2$ (Fig. S3). In comparison with the *operando* XRD (Fig. S5), which still shows $AgCrSe_2$ reflections at 2.1 V, the *ex situ* XRD indicates more complete $LiCrSe_2$ formation. This difference arises from the chronoamperometric hold, which allows further reaction progress toward equilibrium. Therefore, the electrochemical lithiation of $AgCrSe_2$ can be viewed as an intermediate process occurring at different potentials, while the discrepancy between *ex situ* and *operando* results reflects kinetic limitations during continuous discharge. The XRD pattern at 2.1 V does not show a shift of the (003) peak, as reported by Peng *et al.*[20] Instead, the $AgCrSe_2$ reflections disappear and $LiCrSe_2$ reflections appear. This suggests that phenomena such as Li insertion into the $AgCrSe_2$ lattice to form a $Li_xAg_{1-x}CrSe_2$ solid solution do not occur. Rather, this reaction appears to be limited to $AgCrS_2$ or to chemical reduction conditions. Upon further reduction to 1.5 V, the $LiCrSe_2$ peaks intensified, and metallic Ag peaks emerged. This supports the interpretation that the first potential plateau corresponds to the insertion of one lithium per formula unit, involving Ag extrusion and Li intercalation into the interlayer.

At 0.8 V, the $LiCrSe_2$ peaks disappeared, while peaks for Li_2Se appeared, signaling the proposed conversion reaction. However, there is no clear evidence of Cr metal formation. This could be due to (1) the Cr-metal peaks overlapping with the Ag-metal peaks, making it difficult to observe, and/or (2) insufficient Cr growth to be detected by XRD, which aligns with the EDS results (Fig. S2). At 0.1 V, the Li_2Se peaks persisted with slightly increased intensity, while the metallic Ag peaks shifted

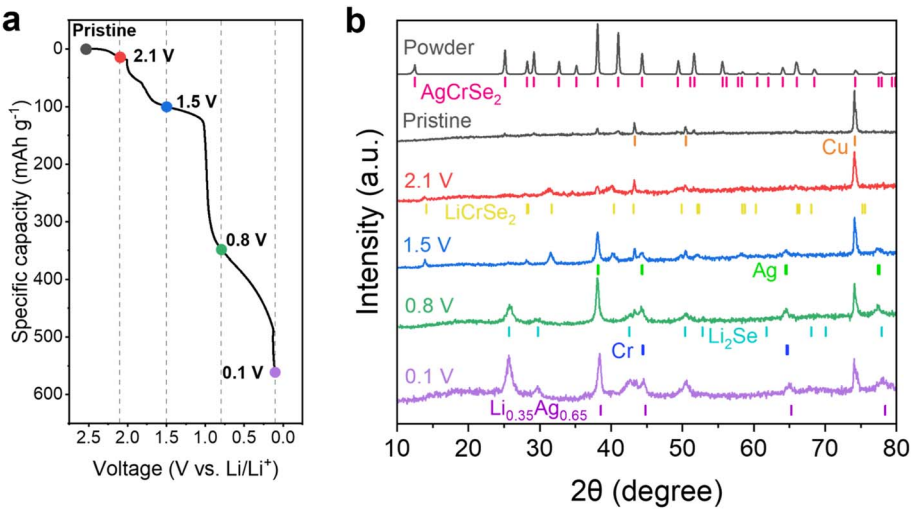

Fig. 4 *Ex situ* XRD of $AgCrSe_2$ electrodes during the first discharge in 1 M $LiClO_4$ in PC. Electrodes were stopped at selected voltages (pristine, 2.1, 1.5, 0.8, 0.1 V). (a) Galvanostatic profile from OCV to 0.1 V with cutoff points indicated. (b) XRD patterns of electrodes collected at these voltages in the 10–80° 2θ range, showing the sequential appearance and disappearance of diffraction peaks as a function of discharge potential.

to higher diffraction angles, consistent with Li–Ag alloy formation due to the incorporation of smaller Li atoms into Ag.

Peng *et al.* reported that chemical lithiation of $AgCrS_2$, a compositionally and structurally related layered chalcogenide with the same *R*3*m* space group symmetry.[20] The proposed mechanism suggests only partial Ag-extrusion and Li-intercalation leading to the formation of a (Li–Ag)CrS_2 phase as indicated by changes in interlayer spacing from XRD measurements. However, in this study, the interlayer (006) peak at 25° remains unchanged in both *ex situ* and *operando* XRD (Fig. S5), indicating that electrochemical lithiation of $AgCrSe_2$ does not result in the formation of a (Li–Ag)$CrSe_2$ phase. Instead of a peak shift, which would indicate a solid solution phase, the *operando* XRD results show a gradual evolution: initially, the $AgCrSe_2$ peak at 41° is present, followed by the coexistence of peaks at 41° ($AgCrSe_2$) and 40° ($LiCrSe_2$), and finally, only the 40° ($LiCrSe_2$) peak remains until reaction II completes. In addition, the peak at 38° exhibits broadening and a slight increase in intensity, suggesting a phase transition. Since both $AgCrSe_2$ and metallic Ag have reflections at this position, the broadening may indicate the formation of nanosized Ag particles, consistent with a conversion reaction.

3.4. Surface chemistry changes during lithiation

Ex situ XRD confirms the formation of $LiCrSe_2$, Ag, and Li_2Se during the lithiation process. Due to the similar XRD peak positions of Cr and Li–Ag alloy with Ag, these phases are difficult to confirm by XRD alone. To verify their presence and finalize the lithiation mechanism, X-ray photoelectron spectroscopy (XPS) was conducted. XPS calibration was performed using the C–C single bond peak, set at 285 eV (Fig. S6a). The pristine C 1s spectrum was deconvoluted into five peaks: C=C (283.8 eV), C–C (285 eV), C–O (286.4 eV), C=O (289.4 eV), and C–F_2 (290.3 eV). The C–F_2 peak originates from the PVDF binder used in the composite slurry electrode, while the other peaks arise from both acetylene black and the PVDF backbone.[27] In *ex situ* samples, the C=C peak weakens, while C=O and C–O peaks intensify, suggesting the introduction of an electrolyte on the surface, covering the acetylene black. The pristine O 1s spectrum includes peaks for O–C (533.1 eV), O=C (531.9 eV), and SeO_2 (530.4 eV).[28] For *ex situ* samples, with the addition of carbonate electrolyte and ClO_4^- salt, the peak at 533.1 eV is significantly enhanced. The introduction of the ClO_4^- anion is confirmed by the chlorine 2p spectrum at 208.5 eV ($2p_{3/2}$) and 210.0 eV ($2p_{1/2}$) in Fig. S6c. In addition, a novel peak below 530 eV could be attributed to the formation of metal oxides (*e.g.*, Ag_2O, Li_2O) when the highly reduced *ex situ* samples were exposed to ambient air, as also confirmed by the EDS oxygen maps (Fig. S4). The O–C and O=C peaks are confirmed from the C 1s spectrum, and the SeO_2 peak is identified in the Se 3d spectrum (Fig. 5c).

Fig. 5 shows the evolution of the chemical states and bonding environments of the elements composing the active electrode materials upon lithiation. Pristine chromium 2p spectrum consists of peaks at $2p_{1/2}$ (596.1 eV) and $2p_{3/2}$ (576.8 eV). The Cr $2p_{3/2}$ peak at 576.8 eV originates from the Cr^{3+} ion in $AgCrSe_2$ and this matches with other Cr^{3+}-containing materials such as Cr(III) oxide (575.7 eV) and Cr(III) hydroxide (577.7 eV).[29] The peak position remains unchanged when reduced to 2.1 V, indicating that reaction I is not yet complete. At 1.5 V, where reaction II is considered to have progressed, both $2p_{1/2}$ and $2p_{3/2}$ shift to a lower binding energy of 576.1 eV indicating some degree of Cr^{3+} reduction. When the entire reduction process is finished, the peak is centered at 575.9 eV. Given that metallic chromium (Cr(0)) is located at a lower binding energy than Cr^{3+}, the result suggests the reduction of Cr^{3+} to Cr^0. This behavior aligns with the conversion reaction ($LiCrSe_2 + 3Li^+ + 3e^- \rightarrow Cr + 2Li_2Se$), as confirmed by XRD.

Ag 3d peaks appear at 373.6 eV ($3d_{3/2}$) and 367.6 eV ($3d_{5/2}$). Upon reduction to 2.1 V and 1.5 V, a subtle increase in binding energy is observed. Since Ag^0 generally exhibits a higher binding energy than Ag^+, this shift suggests the reduction of Ag^+ to Ag metal. At 0.8 V and 0.1 V, no Ag-related peaks are detected.[30] This absence is likely due to a decrease in Ag atomic %, which may result from the oxidation of Ag or the removal of Ag particles during *ex situ* sample preparation.

The pristine Se 3d spectrum exhibits peaks corresponding to SeO_2 (58.3 eV) and $AgCrSe_2$ (53.6 eV). The Se 3d spectrum is not deconvoluted into $3d_{3/2}$ and $3d_{5/2}$ components because the typical spin–orbit splitting of Se 3d is only 0.86 eV,[31] which is significantly smaller than the 4.7 eV binding energy difference arising from different bonding environments. After lithium introduction, a distinct Li 1s peak appears at 55.7 eV which matches with other Li^+-containing species such as LiO. The peak shift of Se 3d to lower energy indicates a change in the Se bonding environment even at a low state of lithiation (2.1 V). This suggests that modifications in $AgCrSe_2$ begin occurring during the initial stage of the lithiation reaction. The Li 1s peak shifts to lower binding energies, indicating a transition from ionic lithium to metallic lithium during Ag–Li alloy formation, well before the theoretical lithium deposition potential.

3.5. Li ion diffusion behavior during lithiation

Peng *et al.* report an increase in the ionic conductivity of Li_x-$Ag_{1-x}CrS_2$ with Li content x, reaching a maximum conductivity at $x = 0.31$.[20] Ionic conductivity (σ) and the diffusion coefficient (D) are directly related by the Nernst–Einstein equation:

$$\sigma = \frac{nz^2e^2D}{k_BT} \quad (5)$$

We obtained the diffusion coefficient using two methods: galvanostatic intermittent titration technique (GITT) and electrochemical impedance spectroscopy (EIS). GITT was employed to calculate the apparent diffusion coefficient during lithiation and delithiation. Unlike the trend reported by Peng *et al.*, the diffusion coefficient fluctuates but generally decreases in region I (3.0–1.5 V), where lithiation induces a phase transition from $AgCrSe_2$ to $LiCrSe_2$ (Fig. S7).[20]

We also determined the diffusion coefficient using EIS with the method described in Ref. 32, based on the Warburg constant (σ_W). σ_W was obtained from the slope of the real part of

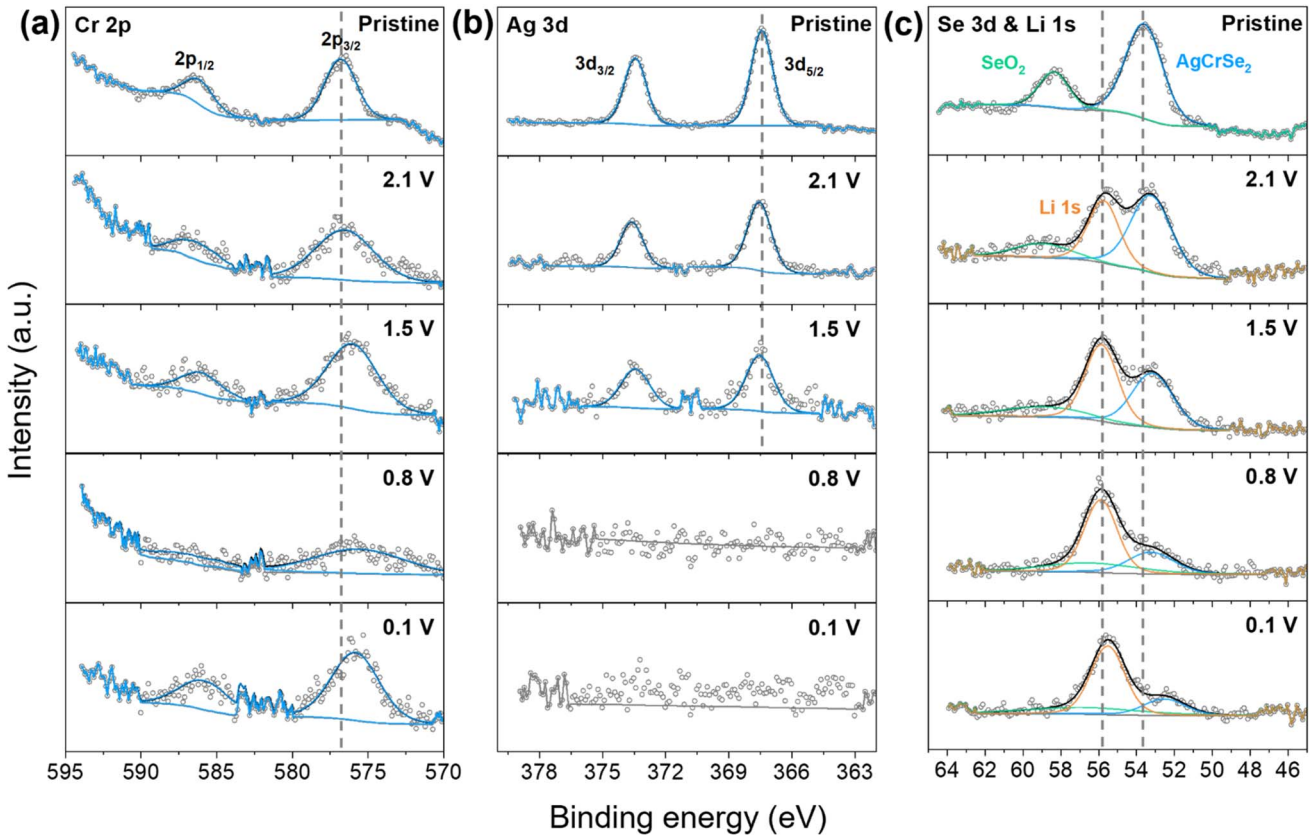

Fig. 5 *Ex situ* XPS core spectra obtained from $AgCrSe_2$ electrodes discharged to different cutoff voltages (pristine, 2.1, 1.5, 0.8, and 0.1 V) in 1 M $LiClO_4$ in PC: (a) Cr 2p, (b) Ag 3d, and (c) Se 3d and Li 1s. The spectra reveal progressive reduction of Cr^{3+}, the emergence and loss of Ag signals, and shifts in Se and Li peaks reflecting changes in bonding environments during lithiation.

the impedance (Z') plotted against the inverse square root of frequency. The diffusion coefficient is then calculated using the equation:

$$\sigma_W = \frac{RT}{n^2F^2A\sqrt{2}}\left(\frac{2}{D^{0.5}C}\right) \quad (6)$$

and plotted as a function of x in $Li_xAgCrSe_2$, which denotes the state of charge. The decreasing trend in the diffusion coefficient during lithiation is further confirmed by EIS within the lithium intercalation voltage range (region I), down to 1.4 V (Fig. S8).

4. Conclusions

In this study, we employed electrochemical characterization and *ex situ* characterization to investigate the electrochemical lithiation mechanism of layered $AgCrSe_2$ and $CuCrSe_2$. The results reveal a three-step process involving the total transfer of ~6.6 Li^+ per $AgCrSe_2$ and 5.7 Li^+ per $CuCrSe_2$. In the first step, Ag extrusion from $AgCrSe_2$ is combined with Li^+ intercalation to yield $LiCrSe_2$ decorated with Ag nanoparticles. The second step is the conversion of $LiCrSe_2$ into Li_2Se and Cr. In the third and final step, the extruded Ag reacts with Li^+ at approximately 0.13 V to form a Li–Ag alloy. $CuCrSe_2$ follows only the first two steps due to the absence of Li–Cu alloying. In both materials, electrochemical reduction is accompanied by significant microstructural reconstruction, Ag redistribution, and changes in Se bonding environments. Measurements of Li-ion diffusivity indicate a general decrease in diffusion coefficient during Ag–Li exchange. This behavior is in contrast to the concept of room-temperature superionic conductivity achieved through the 'pillar effect' reported in (Ag–Li)CrS_2, suggesting that the substitution of Se for S fundamentally alters the transport mechanism. These findings provide the electrochemical reduction mechanisms of the $MCrX_2$ family of materials in the presence of alkali ions and offer guidance for the design of layered transition-metal chalcogenides as high-energy-density lithium-ion battery electrodes or electrolytes.

Conflicts of interest

There are no conflicts to declare.

Data availability

Data from this work is openly available at https://doi.org/10.5281/zenodo.17244893.

Supplementary information: supplementary figures and tables including additional electrochemical data, *ex situ* SEM/EDS characterization, operando XRD patterns, XPS spectra, impedance and GITT-based kinetic analyses, and Rietveld refinement results. See DOI: https://doi.org/10.1039/d5ta08061d.

Acknowledgements

This material is based upon work supported by the National Science Foundation under Grants No. DMREF-2119377 (S. M., N. P. H. and V. A.) and DMREF-2118463 (M. T. R. and A. Z.). This work was performed in part at the Analytical Instrumentation Facility (AIF) at North Carolina State University, which is supported by the State of North Carolina and the National Science Foundation (award number ECCS-2025064). The AIF is a member of the North Carolina Research Triangle Nanotechnology Network (RTNN), a site in the National Nanotechnology Coordinated Infrastructure (NNCI).

References

1 J. W. Choi and D. Aurbach, *Nat. Rev. Mater.*, 2016, **1**, 16013.
2 X. Zuo, J. Zhu, P. Müller-Buschbaum and Y.-J. Cheng, *Nano Energy*, 2017, **31**, 113–143.
3 T. Wang, S. Chen, H. Pang, H. Xue and Y. Yu, *Adv. Sci.*, 2016, **3**, 1600289.
4 W. Choi, Y. S. Choi, H. Kim, J. Yoon, Y. Kwon, T. Kim, J.-H. Ryu, J. H. Lee, W. Lee, J. Huh, J. M. Kim and W.-S. Yoon, *Chem. Mater.*, 2021, **33**, 1935–1945.
5 Y.-Z. Wang, X.-Y. Shan, D.-W. Wang, Z.-H. Sun, H.-M. Cheng and F. Li, *Joule*, 2018, **2**, 1278–1286.
6 X. Li, J. Zhi, Y. Xie, Y. Huang and H. Li, *RSC Adv.*, 2015, **5**, 85857–85863.
7 R. Bhandavat, L. David and G. Singh, *J. Phys. Chem. Lett.*, 2012, **3**, 1523–1530.
8 F. Han, J. Yue, X. Fan, T. Gao, C. Luo, Z. Ma, L. Suo and C. Wang, *Nano Lett.*, 2016, **16**, 4521–4527.
9 D. Su, D. Zhou, C. Wang and G. Wang, *Adv. Funct. Mater.*, 2018, **28**, 1800154.
10 G. Xiang, X. Yan, X. Xiong, Y. Zong, S. Aziz, Z. Zhu and Y. Wu, *Mater. Today Energy*, 2025, **51**, 101894.
11 P. Yu, S. Sun, C. Sun, C. Zeng, Z. Hua, N. Ahmad, R. Shao and W. Yang, *Adv. Funct. Mater.*, 2024, **34**, 2306939.
12 Y. Fujita, K. Münch, T. Asakura, K. Motohashi, A. Sakuda, J. Janek and A. Hayashi, *Chem. Mater.*, 2024, **36**, 7533–7540.
13 F. Wu, J. T. Lee, Y. Xiao and G. Yushin, *Nano Energy*, 2016, **27**, 238–246.
14 J. H. Um, A. Jin, X. Huang, J. Seok, S. S. Park, J. Moon, M. Kim, S. H. Kim, H. S. Kim, S.-P. Cho, H. D. Abruña and S.-H. Yu, *Energy Environ. Sci.*, 2022, **15**, 1493–1502.
15 D. You, W. Yang, Y. Liang, C. Yang, Y. Yu, Z. Zhu, X. Li, Y. Zhang and Y. Zhang, *Adv. Funct. Mater.*, 2025, **35**, 2421900.
16 Y. Ma, Y. Ma, G. Giuli, H. Euchner, A. Groß, G. O. Lepore, F. d'Acapito, D. Geiger, J. Biskupek, U. Kaiser and H. M. Schütz, *Adv. Energy Mater.*, 2020, **10**, 2000783.
17 J. Ding, M. Towhidur Rahman, C. Mao, J. L. Niedziela, D. Bansal, A. F. May, D. L. Abernathy, Y. Ren, A. Zevalkink, O. Delaire, *et al.*, *Phys. Rev. Mater.*, 2025, **9**, 035402.
18 M. T. Rahman, N. P. Holzapfel, K. Ciesielski, W. Guetari, E. Toberer, V. Augustyn and A. Zevalkink, *Chem. Mater.*, 2025, **37**, 6718–6726.
19 M. T. Rahman, K. Ciesielski, J. Pelkey, A. K. M. A. Shawon, E. Toberer and A. Zevalkink, *J. Phys.: Energy*, 2025, **7**, 035016.
20 J. Peng, Y. Liu, Y. Pan, J. Wu, Y. Su, Y. Guo, X. Wu, C. Wu and Y. Xie, *J. Am. Chem. Soc.*, 2020, **142**, 18645–18651.
21 D. Wu, S. Huang, D. Feng, B. Li, Y. Chen, J. Zhang and J. He, *Phys. Chem. Chem. Phys.*, 2016, **18**, 23872–23878.
22 A. Khan, M. Orbay, N. Dupré and E. Gautron and others, *Energy Storage Mater.*, 2024, **70**, 103431.
23 D. A. Skoog, F. J. Holler and S. R. Crouch, *Principles of Instrumental Analysis*, Cengage Learning, Boston, 7th edn, 2018, pp. 914–915.
24 A. D. Pelton, *Bull. Alloy Phase Diagrams*, 1986, **7**, 133–136.
25 P. F. Bongers, C. F. Van Bruggen, J. Koopstra, W. P. F. A. M. Omloo, G. A. Wiegers and F. Jellinek, *J. Phys. Chem. Solids*, 1968, **29**, 977–984.
26 B. Li, H. Wang, Y. Kawakita, Q. Zhang, M. Feygenson, H. L. Yu, D. Wu, K. Ohara, T. Kikuchi, K. Shibata, T. Yamada, X. K. Ning, Y. Chen, J. Q. He, D. Vaknin, R. Q. Wu, K. Nakajima and M. G. Kanatzidis, *Nat. Mater.*, 2018, **17**, 226–230.
27 P. Viswanath and M. Yoshimura, *SN Appl. Sci.*, 2019, **1**, 1519.
28 R. Ciceo-Lucacel, T. Radu, O. Ponta and V. Simon, *Mater. Sci. Eng., C*, 2014, **39**, 61–66.
29 M. C. Biesinger, B. P. Payne, A. P. Grosvenor, L. W. M. Lau, A. R. Gerson and R. S. C. Smart, *Appl. Surf. Sci.*, 2011, **257**, 2717–2730.
30 C. D. Wagner, *NIST Technical Note 1289: the NIST X-Ray Photoelectron Spectroscopy (XPS) Database*, National Institute of Standards and Technology, Washington, DC, 1991.
31 J. F. Moulder, W. F. Stickle, P. E. Sobol and K. D. Bomben, *Handbook of X-Ray Photoelectron Spectroscopy*, Perkin-Elmer Corporation, Eden Prairie, MN, 1992.
32 R. Vedalakshmi, S. Velu, H.-W. Song and N. Palaniswamy, *Corros. Sci.*, 2009, **51**, 1299–1307.

